European Rotorcraft Forum

AERODYNAMICS OF SMALL ROTORS IN HOVER AND FORWARD FLIGHT

Felix Lößle, Anna A. Kostek, Clemens Schwarz, Rainer Schmid, Anthony D. Gardner, Markus Raffel
Institute of Aerodynamics and Flow Technology, German Aerospace Center (Germany)

Abstract
A wind tunnel test of eleven two- and three-bladed small-scale rotors was conducted in an open-jet, low-speed wind tunnel. The goal was to study the influence of number of blades, blade pitch and geometry on the hover performance. Two rotors were also studied in forward flight with varying rotational speeds, rotor tilt angles and flow velocities covering a wide range of operating conditions. The experimental results were used to develop a simple, empirical model of the studied rotor based on dimensionless quantities. The model can be used in the preliminary design of multicopters. The performance measurements were supplemented with optical background-oriented schlieren (BOS) measurements to visualize the blade tip vortices in the rotor wake in order to gain a better understanding of the flow state. Simulations with DLR's free wake unsteady panel code (UPM) were carried out for comparison.

NOMENCLATURE

A	Rotor disc area, m^2
A_{ref}	Reference area, m^2
c	Chord length, m
C_d	Drag coefficient
C_{d0}	Zero-lift drag coefficient
C_T	Thrust coeff., $T/(\rho A(\Omega R)^2)$
C_P	Power coeff., $P/(\rho A(\Omega R)^3)$
C_Y	Tangential force coeff., $F_y/(\rho A(\Omega R)^2)$
D	Drag force, N
D	Rotor diameter, m
F_{res}	Resultant force, N
F_y	Tangential force, N
FM	Figure of merit
g	Gravitational constant, $9.81\,m/s^2$
L	Lift force, N
m	Mass, kg
MAC	Mean aerodynamic chord, m
n	rotational frequency, rpm
N_b	Number of rotor blades
P	Rotor power, W
r	Radial coordinate, m
R	Rotor radius, m
Re	Reynolds number
T	Rotor thrust, N
V_∞	Freestream velocity, m/s
z	Axial coordinate, m
α	Tilt angle, $^\circ$
Γ	Circulation
κ	Induced power factor
μ	Advance ratio, $V_\infty \cos(\alpha)/(\Omega R)$
ρ	Air density, kg/m^3
σ	Rotor solidity
Φ	Angle of incidence, $^\circ$
Ψ	Azimuth angle, $^\circ$
Ω	Rotational frequency, 1/s

Abbreviations

BOS	Background-oriented schlieren
BVI	Blade vortex interaction
DLR	German Aerospace Center
PIV	Particle image velocimetry
RTG	Rotor test facility Göttingen
UAV	Unmanned aerial vehicles
UPM	Unsteady panel method

1. INTRODUCTION

Due to the increased use of unmanned aerial vehicles (UAVs) in recent years, the aerodynamics of small rotors is a subject of growing interest. Although a lot of research has been dedicated to helicopter aerodynamics, it is not directly applicable to UAV rotors. The major differences are: (i) UAV rotors operate in the regime of low Reynolds numbers, (ii) UAV rotors are typically rigid and thrust control is realized by the adjustment of rotational speed and (iii) UAV rotors are usually not linearly twisted and have

strongly varying spanwise chord distributions.

Several experiments and simulations in hover and forward flight were carried out in recent years to investigate the aerodynamics of small-scale rotors. The effect of low Reynolds numbers on the rotor efficiency was experimentally investigated by Ramasamy et al. (2008)[1] for hover. They studied rectangular, linearly tapered and twisted rotor blades, noticing that the figure of merit *FM* for small-scale rotors operating at low Reynolds numbers is significantly lower than the *FM* for large rotors operating at higher Reynolds numbers, even though conventional rotor design strategies hold for small-scale rotors. Ramasamy et al. (2007)[2] and Hein and Chopra[3] applied laser flow visualization and particle image velocimetry (PIV) to visualize the rotor wake, and found much thicker and more turbulent wake sheets and larger viscous core sizes of the tip vortices compared to helicopters, causing the lower *FM*. Lakshminarayan and Baeder[4] performed compressible Reynolds-averaged Navier-Stokes calculations for the rotors studied by Ramasamy et al.[1,2] and found good agreement with the experiment.

The effect of the spanwise distribution of airfoil geometry and twist on hover efficiency was investigated by Hein and Chopra[3] using cambered flat plates for low Reynolds numbers. Ramasamy et al. (2010)[5] studied the effect of blade twist on rotor performance and wake structure. They found that the benefit of highly-twisted blades only results at larger thrust coefficients. Numerical investigations for the optimization of spanwise chord and twist distribution of small rotors in hover were carried out by Klimczyk[6] and Bohorquez et al.[7], among others. Milluzzo and Leishman[8] studied the influence of blade twist on the rotor wake applying PIV.

Experiments in forward flight were conducted for a wide range of operational conditions (inflow velocity, rotational speed, tilt angle). The investigations of Serrano et al.[9], Kolaei et al.[10] and Simmons and Hatke[11] focused on the comparison of different rotors and operational conditions, whereas the studies of Krebs et al.[12], Theys et al.[13] and Yang, H. et al.[14] dealt rather with the comparison of experiment and simulation. Ye et al.[15] and Pollet et al.[16] showed that an aerodynamic model can be derived from experimental results. They demonstrated the application of such empirical models in the design process of multicopters[17,16].

The rotor wake of small-scale rotors is of particular interest in forward flight, as blade-vortex interaction (BVI) can occur under certain flight conditions generating high amplitude impulsive noise. However, there are few studies dealing with experimental investigation of wakes in forward flight. The wake of a model helicopter was studied by Ghee and Elliott[18] using laser flow visualization. Lößle et al.[19] demonstrated that background-oriented schlieren (BOS) can be applied to visualize tip vortices of small rotors.

The aim of the current work is to gain a better understanding of the aerodynamics of small rotors in both hover and forward flight. In hover, the influences of rotor pitch, blade number and rotor blade geometry on performance were investigated. For this purpose, thrust and power of eleven different rotors were measured at different rotational speeds. To investigate the aerodynamics in forward flight, two of the rotors were examined in a wide operational range (variation of inflow velocity, rotational speed and rotor tilt angle). Using these data, an empirical model for the rotor was developed based on dimensionless coefficients. Additionally, the tip vortices of the rotor wake were visualized with BOS. This allowed the detection and localization of BVI and helps with the interpretation of performance data. For comparison, simulations with DLR's free wake unsteady panel code (UPM) were carried out.

2. EXPERIMENTAL SETUP

Rotor experiments were conducted in the rotor test facility (RTG) of the German Aerospace Center (DLR) in Göttingen. The RTG is an Eiffel-tunnel with open jet test section. For this test the wind tunnel was equipped with a nozzle with an outlet area of 0.8 m x 1.6 m in order to achieve inflow velocities up to 24 m/s. The nozzle was equipped with Seiferth wings at the nozzle lips to suppress shear layer instability. The rotor was installed with the rotation axis horizontal in the test section and was driven by a 180 W brushless DC motor. For thrust and torque measurements the drive unit was equipped with a strain gauge force sensor and a piezoelectric torque sensor. The motor, force and torque sensor were covered by an aerodynamic fairing to minimize the aerodynamic interference. The rotor and drive unit were mounted on a rotatable platform, allowing to adjust the tilt angle of the rotor shaft. Sketches of the experimental setup and of the assembly of the drive unit are given in Fig. 1 and Fig. 2. In the following a rearward-tilt of the rotor plane is denoted by positive tilt angles α (see also Fig. 3).

A BOS setup was used to study the flowfield of the rotors. A retroreflective foil printed with a randomly distributed dot pattern (1 mm diameter) was attached to the ceiling (not shown in Fig. 1) and illuminated with LED spotlights. The camera system was positioned on the rotatable platform to obtain the same field of view for different tilt angles. To achieve a sufficient sensitivity of the optical setup a large distance between the background and the cam-

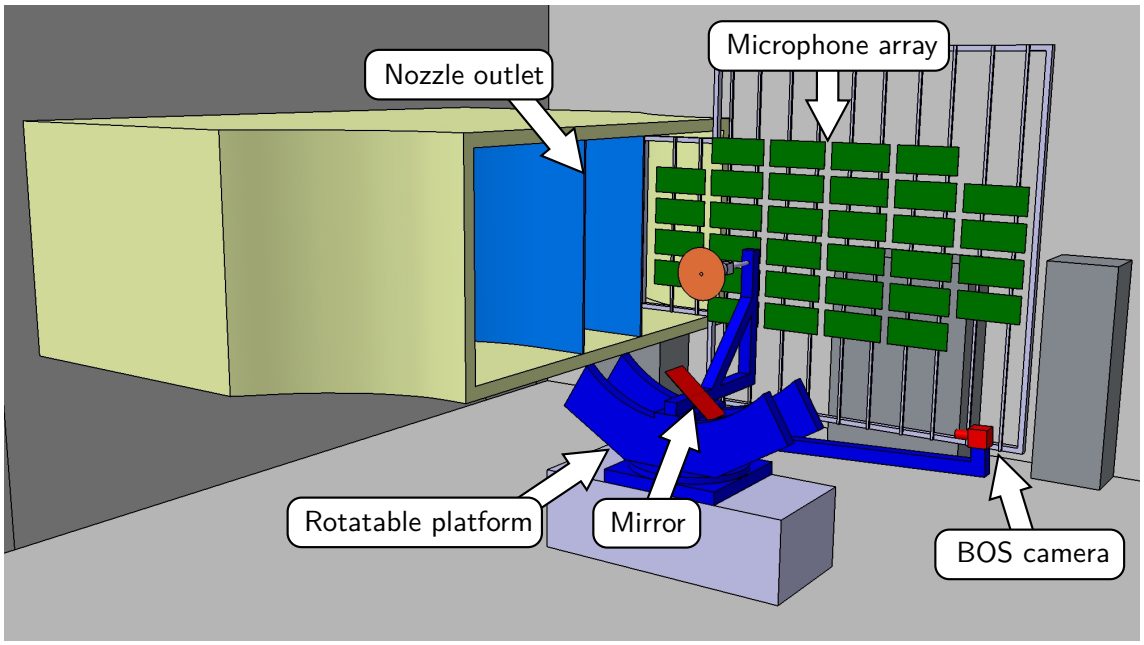

Figure 1: Experimental setup in the rotor test facility (RTG)

Table 1: Geometric parameters of the studied rotors

Series	Name	Symbol	N_b	D [cm]	$\Phi_{0.75}$ [°]	σ	MAC [cm]
Aeronaut CAMcarbon Light	16 x 6 12 x 4.5	● ●	2	40.6 30.5	10.9	0.084	3.3 2.5
Aeronaut CAMcarbon Power	12 x 6 12 x 8 12 x 10	● ● ●	2	30.5	12.7 16.9 21.5	0.066	2.2
KDE Direct	CF125-DP CF125-TP	●	2 3	31.8	6.9	0.076 0.114	2.7
	CF185-DP CF185-TP	●	2 3	47.0	9.5	0.073 0.109	3.6
	CF245-DP CF245-TP	●	2 3	62.2	8.8	0.067 0.100	4.3

era is desirable[20]. For this reason, the light beam was redirected by 90° with a mirror underneath the rotor. Images were taken by a high-speed camera (Phantom VEO 640L) mounted on a cantilever arm. The camera has a resolution of 2560 × 1600 pixels and was equipped with a lens with 135 mm focal length. Both the optical distance between the background and the rotor hub and between the rotor hub and the camera sensor were 2.9 m.

In the measurements, eleven different rotors classified in three series were investigated. The first series comprises two geometrically similar rigid rotors from the manufacturer "Aeronaut" differing in rotor radius (CAMcarbon Light series). The second series consists of three rigid Aeronaut rotors (CAMcarbon Power series) with varying pitch and the same rotor radius, chord and twist distribution. The third series includes six two- and three-bladed rotors with lead-/lag hinges and three different rotor diameters from the manufacturer "KDE Direct". (These rotors were also used in NASA's multicopter test bed.[21]) An overview of the geometric parameters of the studied rotors is given in Tab. 1. For selected rotors the normalized chord and pitch distribution is illustrated in Fig. 4. Although the "KDE Direct" rotors belong to the same series, they differ in the normalized chord distribution (the larger the rotor radius, the higher the aspect ratio). For simplicity the distributions of only one representative of this series is illustrated in Fig. 4.

In the experiment, the rotational frequency n (between 1200 rpm and 5900 rpm), the tilt angle α (between -30° and 30°) and the inflow velocity V_∞ (between 0 m/s and 24 m/s) was varied, covering a wide range of operating conditions. Figure 3 shows the sign orientation and naming convention of

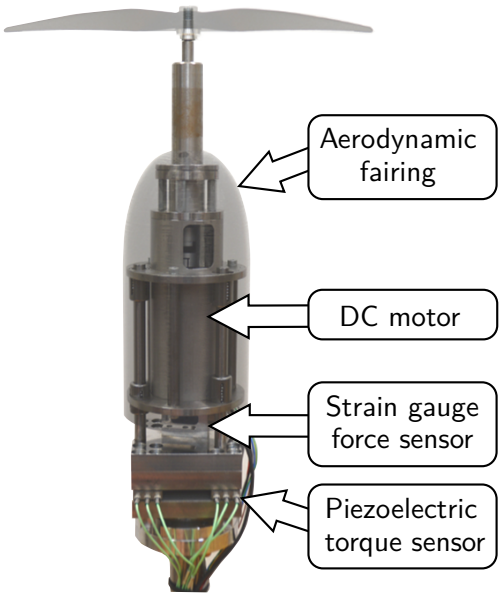

Figure 2: Mechanical setup of the drive unit

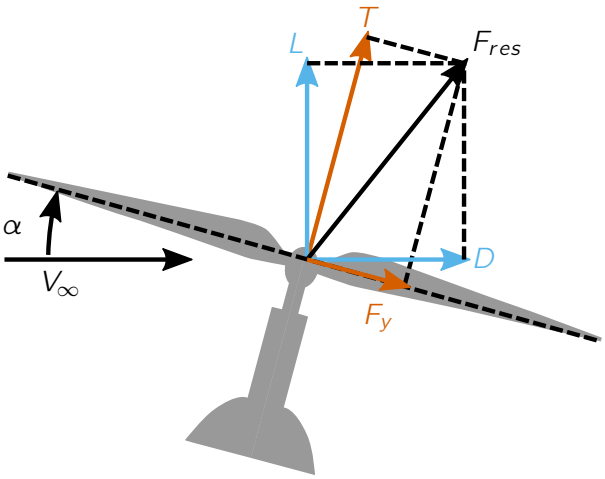

Figure 3: Definition of the aerodynamic forces acting on the rotor

forces acting on the rotor. The measurements for the CAMcarbon Light series, the CAMcarbon Power series and CF125-DP were repeated in order to quantify the stochastic error. The aerodynamic tare loads on the fairing were measured individually. Subtracting the loads from the overall loads yields the net rotor forces.

3. NUMERICAL SETUP

Aerodynamic simulations were performed with DLR's free wake unsteady panel code UPM[22,23,24] to compare them with the experimental results. UPM is a solver for three-dimensional inviscid and incompressible rotor and propeller flow using discrete panels on the surface of the rotor blades. The

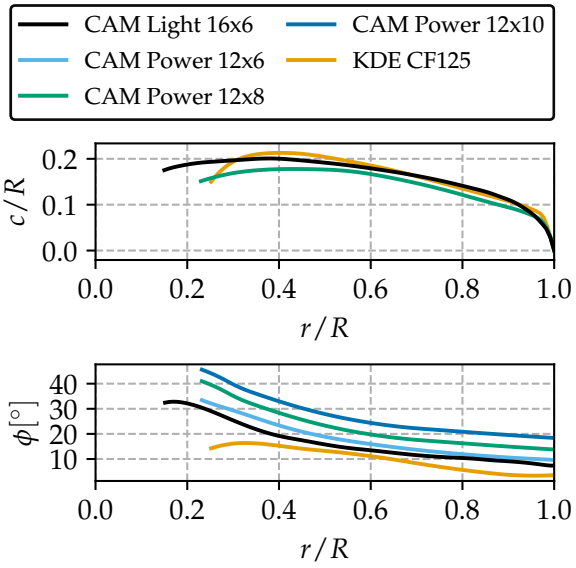

Figure 4: Chord and pitch distribution of the studied rotor blades

rotor blade's thickness is modeled by a source/sink distribution along the blade surface, and the blade lift is modeled by a prescribed doublet distribution. The rotor wake consists of vortex particles inducing a velocity field according to the Biot-Savart law. The rotor wake deforms freely according to the locally induced velocities. Additionally, UPM allows an approximate boundary layer and separation analysis by empirical methods in postprocessing. The viscous corrections do not affect the rotor wake. The rotor geometry was provided by three-dimensional surface scans. Depending on the complexity of the rotor geometry, the airfoils were extracted at 13 to 20 radial positions and approximated with NACA airfoils. Based on these airfoils surface panels for UPM were generated with DLR's panel generation code PANGEN. Figure 6 shows the numerical setup consisting of the rotor, the aerodynamic fairing and the particle wake. Since UPM is an unsteady flow solver, it provides time-resolved thrust and power data as well as the distribution of lift and drag forces causing rotor torque over the rotor plane (see Fig. 5).

4. RESULTS

4.1. Vortex Trajectories

The BOS method visualizes the tip vortex systems due to the spatial inhomogeneity of density induced by tip vortices in the flow. The background shift is the result of the integral of the deflections experienced by a light ray on its way through the density object. Thus, a larger deflection is achieved when the

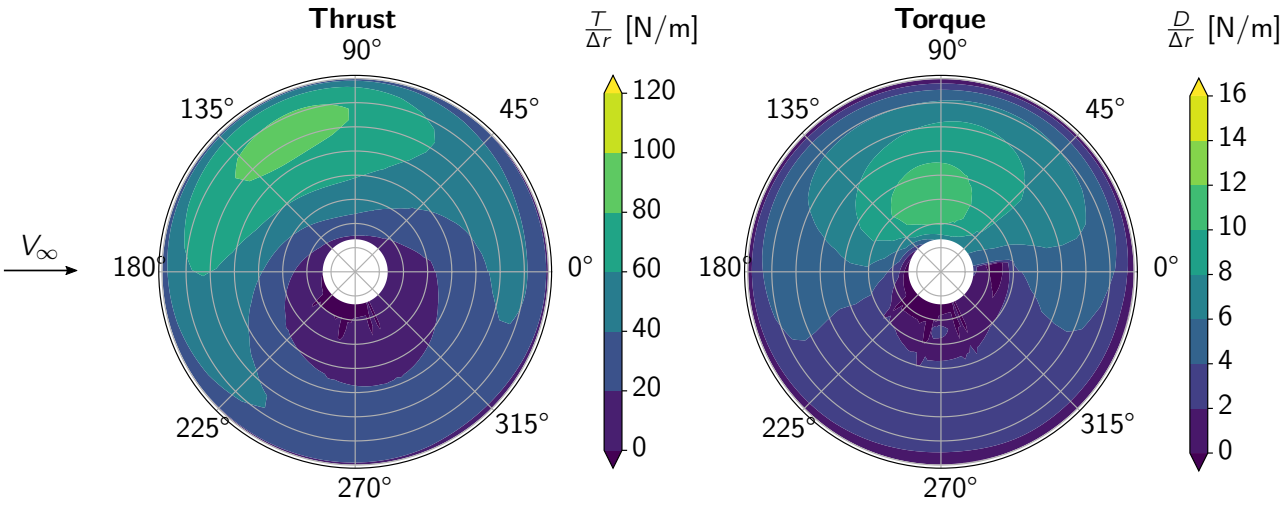

Figure 5: Distribution of lift (left) and drag forces causing torque (right) over the rotor plane for CAMcarbon Light 16x6 at $n = 3600\,\text{rpm}$, $V_\infty = 13\,\text{m/s}$ and $\alpha = -10°$ calculated with UPM, counterclockwise rotating rotor

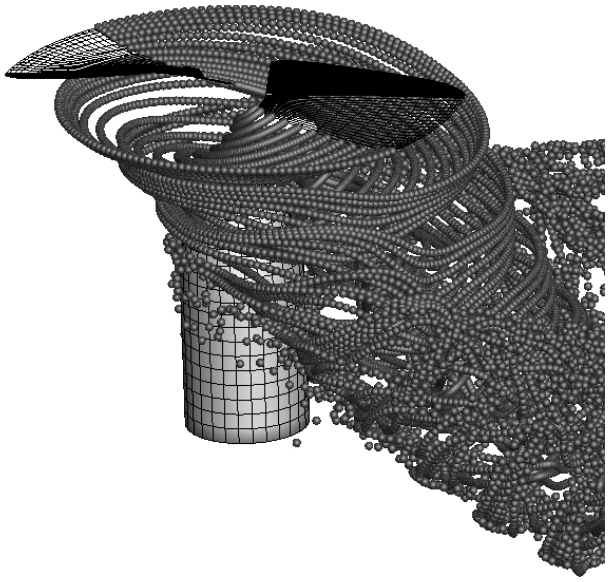

Figure 6: Rotor wake calculated with UPM

light rays run longer parallel to the vortex axis, which is the case at the most outer parts of the curved vortex filaments (see Fig. 7). Snapshots were taken for each 16.4° azimuth angle starting at 0° and with the last image taken at 278.2°.The series was repeated over 18 rotor revolutions, allowing a time-resolved vortex tracking up to a vortex age of about 700°.

First, the results for hover are discussed. Figure 7 (right) shows sample tip vortex trajectories by means of the detected vortex positions over the entire range of vortex ages. Since no images were taken for blade azimuth angles between 278.2° and 360° the trajectories are interpolated in these sections. The axial and radial tip vortex coordinates are separately analyzed in Fig. 8. For vortex ages up to 180°, the tip vortex trajectories show little scatter and are identical for both rotor blades. For higher vortex ages the radial scatter increases and the trajectories of the two blades split up into blade individual vortex trajectories. The vortices trailed from blade 1 have a greater radial distance from the rotor axis than those of blade 2 due to vortex pairing. They reach a minimum radial distance of about 0.79 rotor radii at a vortex age of 450° and are then pushed back to higher radial distances. In contrast, the radial distance of tip vortices generated by blade 2 decreases continuously for growing vortex ages. A difference in motion, albeit weaker, also occurs in the axial direction. The tip vortices of blade 2 sink faster than those of blade 1. This goes along with the tendency observed for radial direction as the vertical velocity is expected to be lower in a greater distance from the rotor's stream tube. In total, this indicates that vortices begin to orbit around each other in pairs, triggered by asymmetry in the trim of rotor blades. Vortex pairing of helicopter rotors was studied, among others, by Schwarz et al.[25].

The comparison with the empirical wake models of Landgrebe[26] and Kocurek and Tangler[27] shows that for the radial coordinate the models are in good agreement with the experimentally detected vortex trajectories for wake ages younger than 180°. For older wake ages the model predictions lie between the measured radial positions of the vortices from blade 1 and 2 and describe the averaged vortex trajectory well. Considering the axial coordinate, the models predict tip vortex trajectories characterized by two sections each with constant but different sink rates. Up to vortex ages of 180° the tip vortices

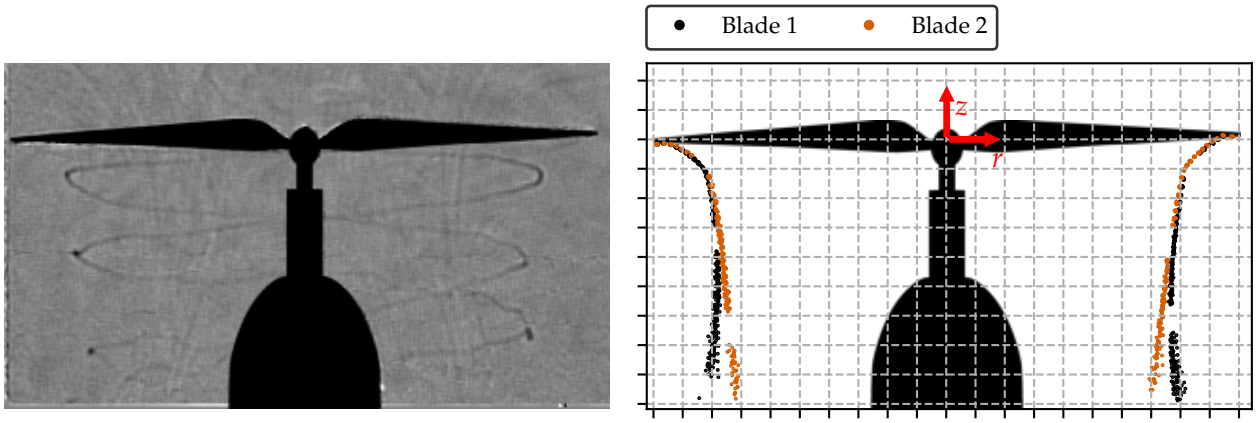

Figure 7: An example for a BOS image (left) and extracted tip vortex positions from a series of 180 images (right) of CAMcarbon Light 16x6 at $n = 4000$

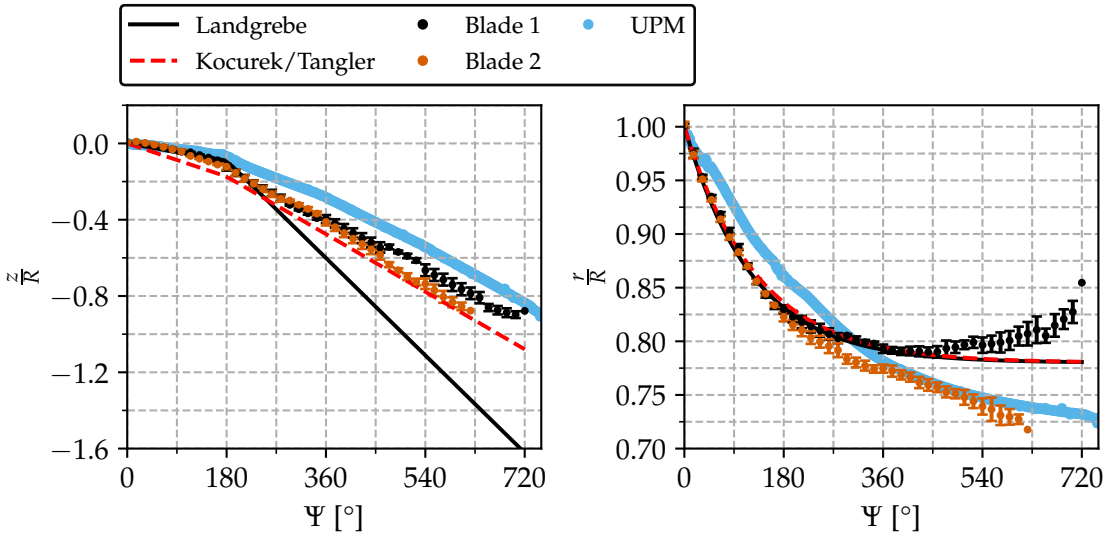

Figure 8: Axial and radial tip vortex coordinates of CAMcarbon Light 16x6 in hover at $n = 4000$ rpm

move downward with moderate velocity. Since the following rotor blade passes the tip vortices which are still in the vicinity of the rotor plane at a vortex age of 180°, an additional vertical velocity is induced and the vortices move downward with higher speed for vortex ages older than 180°. The detected vortex trajectory also shows two sections of constant sink rates. In the first section up to vortex ages of 180°, the model of Landgrebe matches the detected trajectories better than the model of Kocurek and Tangler. In the second section, the model of Kocurek and Tangler reproduces the trajectory correctly while the model of Landgrebe predicts too high sink rates. That is because the CAMcarbon Light 16x6 rotor has an aspect ratio of 7.6, but the model of Landgrebe was developed using rotors with aspect ratios of 13.6 and 18.2[26]. However, Kocurek and Tangler conducted experiments with a wider range of aspect ratios (between 7.1 and 18.2) and accounted for the effect of aspect ratio in their model[27].

The tip vortex trajectories calculated with UPM contract more weakly for $\Psi \leq 360°$ compared to the experiment and models of Landgrebe and Kocurek and Tangler, but for $\Psi > 360°$ the contraction observed in UPM results is stronger. In the axial direction the simulated trajectory also shows two sections with constant sink rate, however the simulated tip vortices sink slightly slower than in the experiment.

Next, the tip vortices in forward flight are studied. Figure 9 illustrates the influence of freestream velocity, tilt angle and rotational speed separately. First, the influence of freestream velocity on the vortex trajectories is discussed. The comparison with hover trajectories reveals that vortex pairing doesn't occur for any studied case in forward flight. Chung et al.[28] studied a two-bladed rotor numerically and found

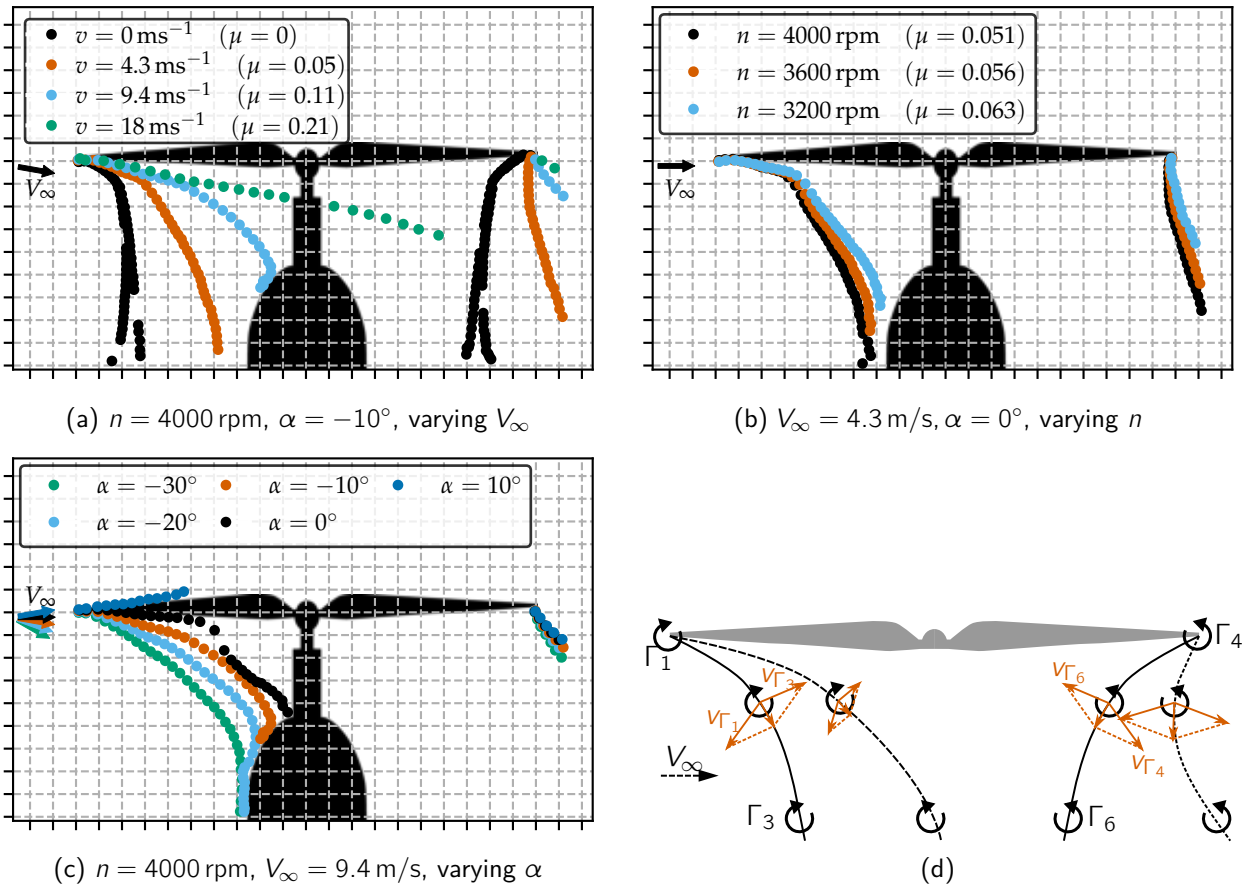

(a) $n = 4000\,\mathrm{rpm}$, $\alpha = -10°$, varying V_∞

(b) $V_\infty = 4.3\,\mathrm{m/s}$, $\alpha = 0°$, varying n

(c) $n = 4000\,\mathrm{rpm}$, $V_\infty = 9.4\,\mathrm{m/s}$, varying α

(d)

Figure 9: Impact of variation of inflow velocity (a), rotational frequency (b) and tilt angle (c) on vortex trajectories; schematic sketch illustrating the impact of lateral flow on the induced velocities of tip vortices (d)

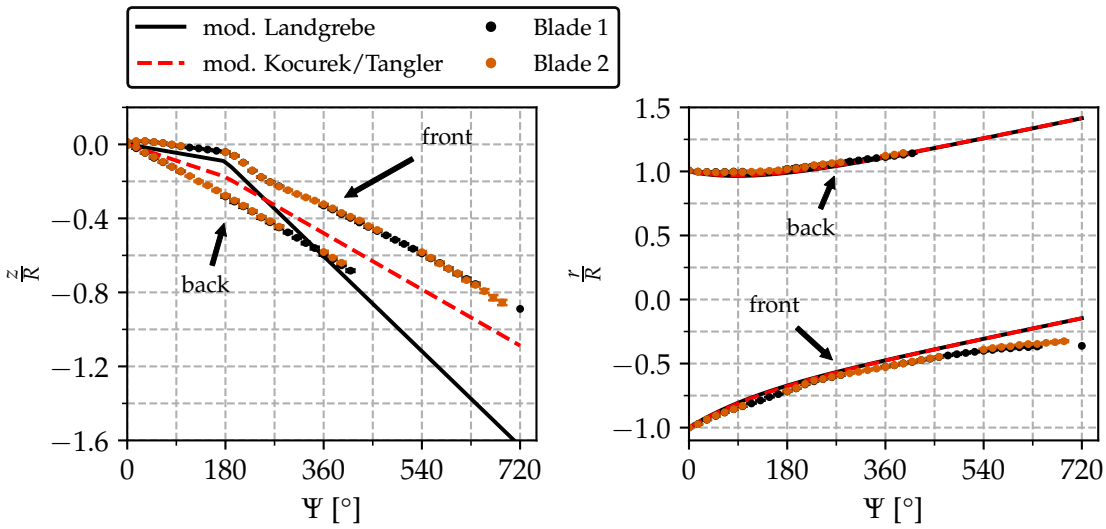

Figure 10: Axial and radial tip vortex coordinates of CAMcarbon Light 16x6 at $n = 4000\,\mathrm{rpm}$, $V_\infty = 4.3\,\mathrm{m/s}$ and $\alpha = 0°$)

that lateral flow has a stabilizing effect on the wake suppressing vortex pairing for advance ratios higher than 0.05. Since the lowest velocity corresponds to an advance ratio of 0.05, the experiment agrees with the result of Chung et al. Furthermore, Fig. 9a shows that the deflection of the vortex trajectories at a vortex age of 180° becomes weaker for higher inflow velocities. The reason for this lies in the distortion of the vortex structure. Since the distance between the vortices in the front region increases with increasing freestream velocity, the velocities of neighboring vortices induced according to the Biot-Savart law are smaller. In addition, the directions of the velocity vectors change. This is schematically illustrated in Fig. 9d.

The reduction in rotational speed is qualitatively similar to the rise of freestream velocity, since both result in an increase of advance ratio. Hence, the effects observed with varying inflow velocity also occur for varying rotational speed.

Finally, the influence of the tilt angle on the vortex trajectories is discussed. It is noted that the results are displayed in a coordinate system fixed to the rotor plane. For high negative tilt angles, both the external flow and the rotor downwash add to increase the convection velocity of the tip vortices. Thus, the vortices move away from the rotor plane at a steep angle immediately after their formation and are not affected by the successive blade. If the tilt angle becomes higher, the vortices remain longer in the vicinity of the rotor plane and thus are stronger affected by the downwash of the following rotor blade. This results in vortex trajectories that sharply drop down at a vortex age of 180° at $\alpha = 0$. For a tilt angle of 10° the rotor induced velocity at the rotor tip is not high enough to overcome the vertical component of the freestream velocity resulting in vortex trajectory located above the rotor. However, the vortices are only visible for a vortex age of up to 180°. This indicates, that they are ingested into the rotor plane by the following rotor blade and eliminated by BVI.

In Fig. 10 the axial and radial tip vortex coordinates are separately analyzed in slow forward flight with $V_\infty = 4.3\,\mathrm{m/s}$, $\alpha = 0°$ and $n = 4000\,\mathrm{rpm}$. For comparison, the models of Landgrebe and Kocurek and Tangler are modified for forward flight by superposition with the freestream velocity. For $\alpha = 0°$ only the radial coordinate is affected by the superposition. The vortices generated in the front are still characterized by two sections with constant sink rates. However, the sink rate in both segments is smaller than predicted by the modified empirical models. In contrast, the vortices in the back sink with constant speed and are not affected by the following blade. As shown in Fig. 9, the reason for this is the deformation of the vortex system by the external flow. The distances between the vortices are stretched in the front and compressed in the back area. This changes both the strength and the direction of the induced velocities of the neighboring vortices. However, these effects are not reproduced by the modified models.

Considering the radial coordinate the vortices both in the front and back follow the modified model of Landgrebe up to $\Psi = 360°$. For higher vortex ages the vortices move backwards more slowly than predicted by the model. This is due to the aerodynamic motor fairing, which is a blunt flow obstacle slowing down the flow.

4.2. Performance in Hover

In hover, the thrust T and the power P of a rotor with rigid blades depend solely on the rotational speed. Figure 11 shows the relation for all studied two-bladed rotors in hover. As expected from theoretical considerations[29], rotor thrust increases with the square and power with the cube of rotational speed.

Next, the dimensionless thrust coefficient C_T and power coefficient C_P defined as

$$(1) \quad C_T = \frac{T}{\rho A(\Omega R)^2}$$

$$(2) \quad C_P = \frac{P}{\rho A(\Omega R)^3}$$

are considered, where ρ is the air density, A the rotor disc area, Ω the rotational frequency and R the rotor radius. These coefficients describe the rotor aerodynamics regardless of the absolute rotor size. Since the thrust increases quadratically and the power cubically with rotational speed, C_T and C_P are also independent of rotational speed and only determined by the rotor geometry. (Provided that the Reynolds number and blade tip Mach number do not vary significantly.)

Considering momentum theory, the ideal power coefficient $C_{P_i deal}$ is given by a function of C_T:

$$(3) \quad C_{P_i deal} = \frac{C_T^{3/2}}{\sqrt{2}}$$

Momentum theory can be extended to account for induced losses (e.g. nonideal inflow, tip losses, finite number of blades) and losses due to parasitic drag. The modified momentum theory is given by

$$(4) \quad C_P = \frac{\kappa C_T^{3/2}}{\sqrt{2}} + \frac{\sigma C_{d0}}{8}$$

where κ is the induced power factor and C_{d0} the zero-lift drag coefficient of the airfoil. A typical value

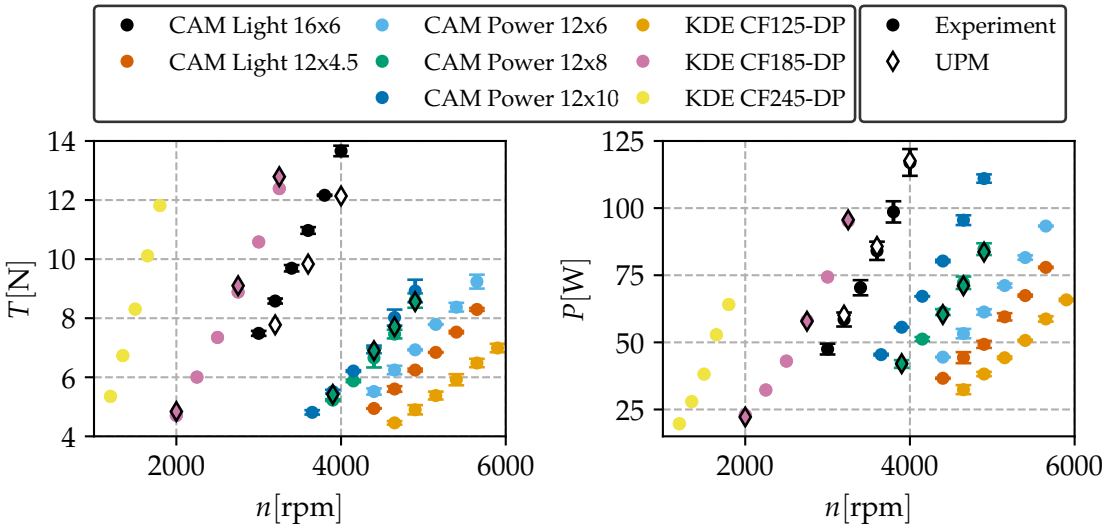

Figure 11: Effect of rotational speed n on rotor thrust T and rotor power P in hover

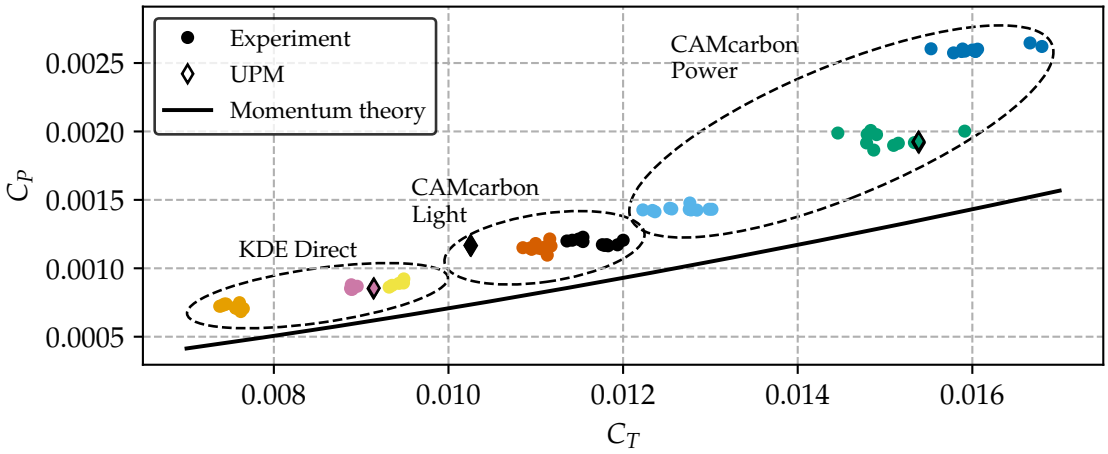

Figure 12: Comparison of experimentally determined thrust and power coefficients of all studied two-bladed rotors to predictions made with momentum theory, color legend as in Fig. 11

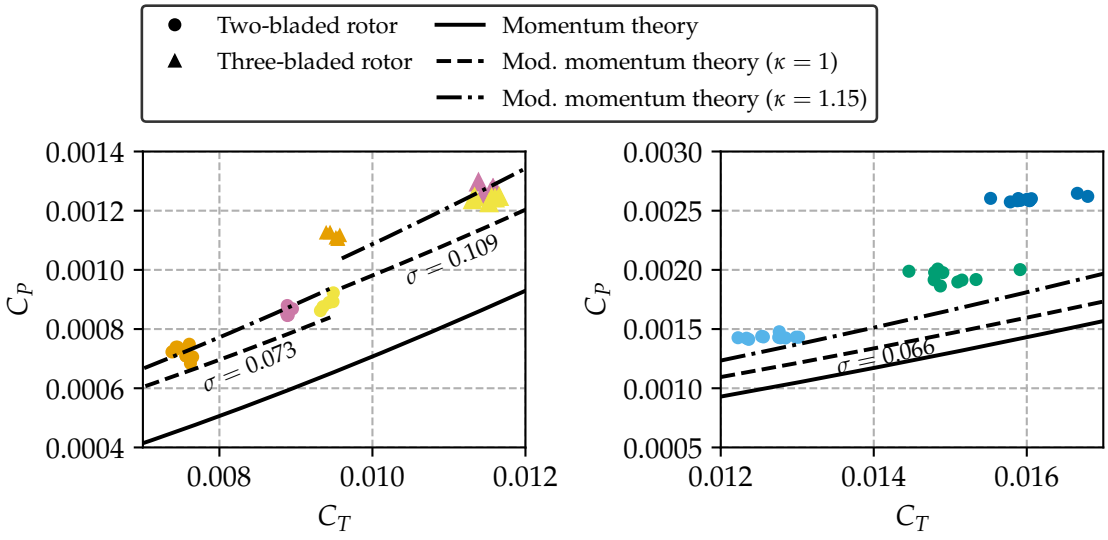

Figure 13: Effect of number of blades (left) and blade pitch (right) on thrust and power coefficients, color legend as in Fig. 11

for helicopter rotors is $\kappa = 1.15$[29]. For $\kappa = 1$ only parasitic drag is considered. In the following a zero-lift drag coefficient of $C_{d0} = 0.02$ is used since this is the zero-lift drag coefficient calculated with XFOIL[30] for a Reynolds number of 10^5 corresponding to typical conditions at 75% of rotor radius. Figure 12 gives a comparison of C_T and C_P of all studied hover cases with the ideal power coefficient. Each dot represents a measurement with individual rotational speed. As predicted by theory, the measurements do not depend on rotational speed and cluster for each rotor. The comparison of the rotors reveals effects of rotor geometry on the thrust and power coefficient: First, since the two rotors of the CAMcarbon Light series are geometrically similar and only vary in absolute dimensions, they are expected to have the same thrust and power coefficients. However, the thrust coefficient of the smaller rotor is about 0.005 smaller than that of the bigger one, due to the rotor hub whose size doesn't scale with the rotor diameter having a stronger relative impact on the smaller rotor.

Second, the effect of the number of rotor blades can be studied considering the two- and three-bladed rotors of the KDE Direct series. Figure 13 shows the measurement results and the prediction of the modified momentum theory of the two-bladed ($\sigma = 0.073$) and three-bladed ($\sigma = 0.109$) KDE Direct rotors. The increased number of rotor blades leads to a rise in C_T and C_P. Since the increase of number of blades leads to an increase in rotor solidity it causes the growth of parasitic drag (see Eq. 4). Hence, the offset from the ideal power coefficient grows with the number of blades. The three-bladed rotors are less efficient than the two-bladed rotors.

Third, the comparison of the CAMcarbon Power rotors reveals the effect of blade pitch. While the measurements of the rotor with the smallest blade pitch (CAMcarbon Power 12x6) are in good agreement with modified momentum theory, power coefficients obtained for the rotor with higher pitch exceed theoretical prediction (see Fig. 13). The disproportionate increase in power with increasing blade pitch indicates flow separation.

Additionally, simulations with UPM were executed for one rotor of each series (CAMcarbon Light 16x6, CAMcarbon Power 12x8 and KDE Direct CF185-DP). Figure 11 and Figure 12 show, that the simulations match both thrust and power in hover. Solely, the thrust of CAMcarbon Light 16x6 is underestimated by the simulation. We assume that inaccuracies in the extraction of airfoils from the 3D scan led to these deviations. Surprisingly, even though viscous effects are not included in UPM and the C_P-C_T-diagram indicates flow separation for CAMcarbon Power 12x8, the UPM simulation matches the measurement.

A measure for rotor efficiency is the figure of merit FM, defined as the ratio of ideal power P_{ideal} to the actual power P_{meas} required:

$$FM = \frac{P_{ideal}}{P_{meas}} = \frac{C_{T,meas}^{3/2}}{\sqrt{2} C_{P,meas}} \quad (5)$$

Considering modified momentum theory (Eq. 4) an approximation for FM is given by:

$$FM = \frac{\frac{C_T^{3/2}}{\sqrt{2}}}{\frac{\kappa C_T^{3/2}}{\sqrt{2}} + \frac{\sigma C_{d0}}{8}} \quad (6)$$

Figure 14 presents the figure of merit derived from the measurement and the approximations of modified momentum theory. What stands out is that for each rotor the measurements don't coincide on one combination of FM and C_T but are aligned along an inclined line in the FM-C_T-diagram. This is due to inaccuracies in the thrust measurements. The dotted lines represent the effect of an erroneous thrust scatter at a constant power reading on C_T and FM, reproducing the inclination of the measurements. Apart from that, the modified momentum theory matches the measurement for the rotors of the KDE Direct series and the CAMcarbon Light series. Rotors with higher C_T have also a higher figure of merit. For the rotors of the CAMcarbon Power series the graph shows that there is a decline in FM with increasing blade pitch indicating flow separation. The figure of merit of rotors without flow separation lie within a range of 0.6 and 0.8. This is within the typical range for full-scale helicopter rotors[29]. Ramasamy et al.[1] studied small-scale rotors in hover at blade tip Reynolds numbers of 35,000 and obtained only figures of merit up to 0.5. As shown by Winslow et al.[31] this is caused a rapid increase of airfoil drag as the Reynolds number decreases below 100,000. A comparison between two- and three-bladed KDE Direct rotors indicates that the three-bladed rotors have higher thrust coefficients, but slightly lower figures of merit than the two-bladed rotors. As shown by the modified momentum theory this is an effect of higher rotor solidity.

4.3. Performance in Forward Flight

Although the agreement of the thrust calculation with the measurement is not as good as for the other simulated rotors, we focus on the performance of the CAMcarbon Light rotors for two reasons. First, the localization of tip vortices was carried out for this rotor. Second, we intend to derive a model for a

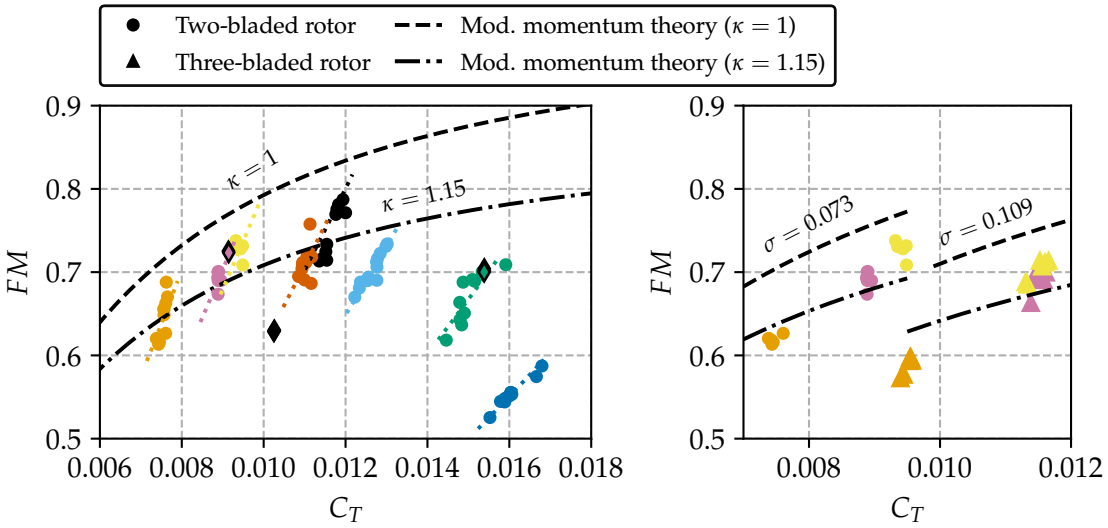

Figure 14: Figure of merit of all studied two-bladed rotors in hover (left); effect of number of blades on the figure of merit (right), color legend as in Fig. 11

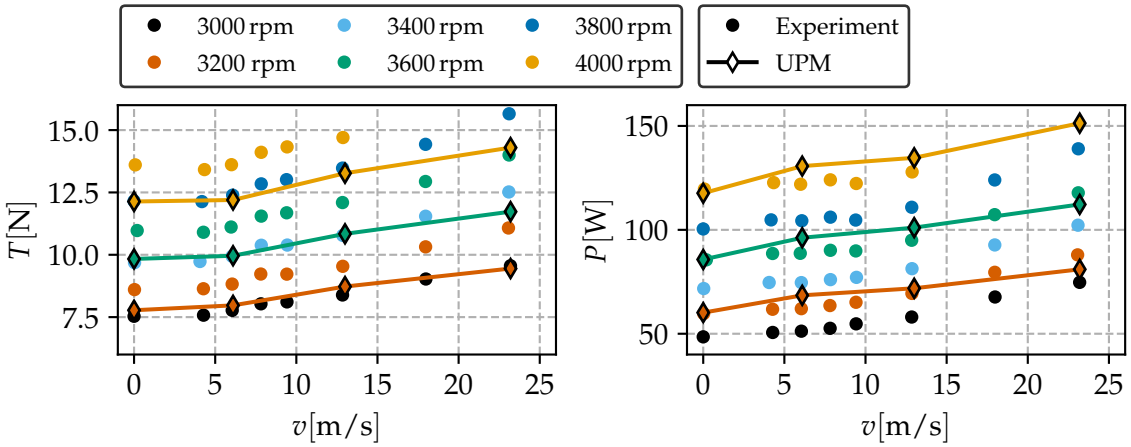

Figure 15: Thrust (left) and power (right) of CAMcarbon Light 16x6 for different rotational speeds and inflow velocities at $\alpha = -10°$

small-scale rotor. Since the two rotors of the CAMcarbon Light series are geometrically similar, these data can be used for cross-validation.

Thrust and power of a rotor in forward flight depend on rotor tilt angle α and flight velocity V_∞, in addition to the rotational speed. In Fig. 15, UPM simulations are compared to the experiment for a rotor tilt angle of -10°. This tilt angle was chosen because in steady forward flight the rotor is usually tilted forward. Moreover, the best agreement between simulation and experiment is expected for negative tilt angles as the forward tilt reduces the blade section angle of attack and thus flow separation. The data shows that UPM underestimates the thrust by approximately 10% for all studied cases of this rotor. However, the simulation reflects the trend correctly for both thrust and power. A more detailed analysis for the comparison of experiment and simulation with UPM and other computational methods in hover and forward flight is given by Kostek et al.[32].

In the following, we derive a systematic description of lift, drag and power of the CAMcarbon Light rotor in forward flight for the whole investigated parameter space. For this an approach, dimensional analysis is applied. In addition to the thrust and power coefficient the tangential force coefficient is defined as

$$C_{Fy} = \frac{F_y}{\rho A(\Omega R)^2}, \tag{7}$$

describing the tangential force F_y in the rotor plane (see Fig. 3). The Buckingham Π theorem[33] indicates that thrust T, power P and tangential force F_y in

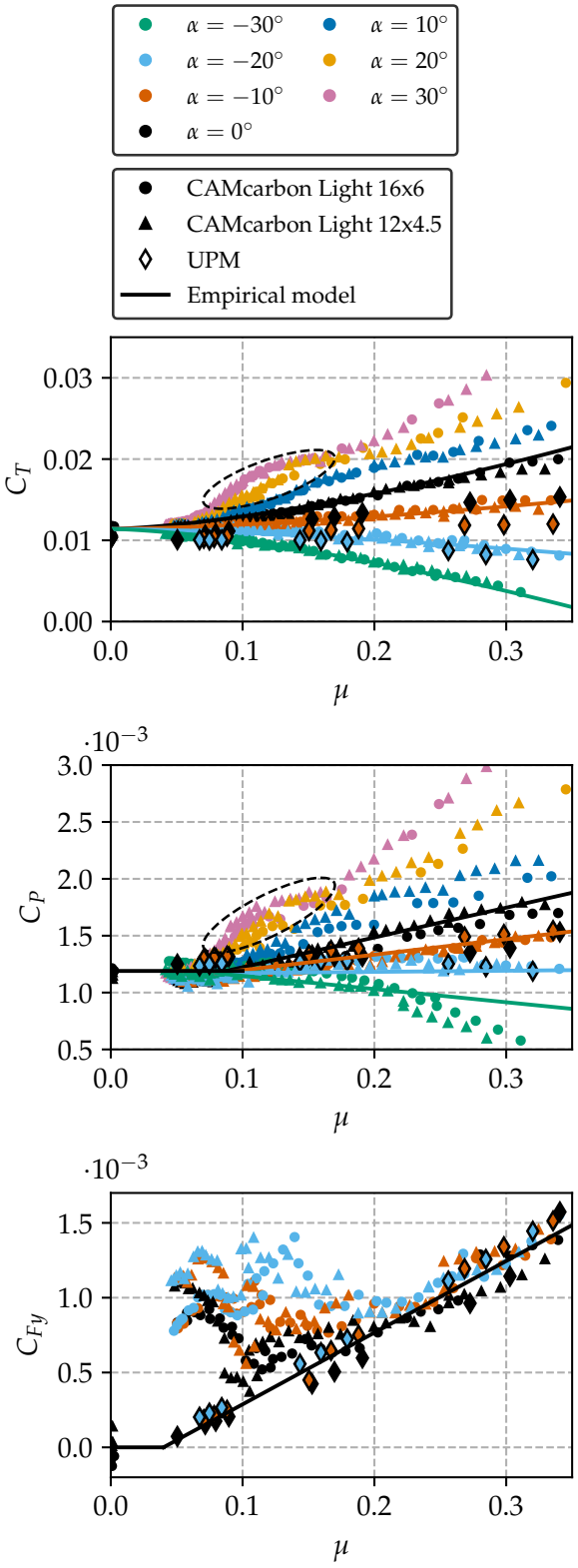

Figure 16: The influence of rotor tilt angle α and advance ratio μ on thrust coefficient C_T, power coefficient C_P and tangential force coefficient C_{Fy}

forward flight are fully characterized by the thrust coefficient C_T, the power coefficient C_P and the tangential force coefficient C_{Fy} as functions of rotor tilt angle α, advance ratio μ and Reynolds number Re. Since blade tip Reynolds numbers reached in the experiment cover a narrow range (between 90,000 and 142,000 calculated at 75% of rotor radius), the effect of Reynolds number on the thrust coefficient can be neglected.

$$(8) \quad C_T = f(\mu, \alpha), C_P = f(\mu, \alpha), C_{Fy} = f(\mu, \alpha)$$

Figure 16 shows the dependencies for all three coefficients, offering a few general observations. As predicted by the Buckingham Π theorem the dimensionless coefficients depend only on advance ratio and tilt angle. Therefore, all measurements are located on tilt-angle-specific curves in the C_T-μ-diagram and C_P-μ-diagram. Moreover, the measurements of both rotors coincide. This is a further proof that the coefficients solely depend on advance ratio and tilt angle. In particular, it verifies that the effect of Reynolds number can be neglected for the studied Re-range.

Considering thrust and power coefficients, Fig. 16 shows that C_T and C_P significantly depend on tilt angle and can both increase and decrease with increasing advance ratio. What stands out in both graphs is the local raise in C_T and C_P for $\alpha \geq 20°$ and $0.07 \leq \mu \leq 0.17$ (marked area in Fig. 16). A possible explanation for this effect can be found in the study of blade tip visualization presented above. In Fig. 9c it is apparent that for $\mu = 0.11$ and $\alpha \geq 10°$ the flow through the rotor disk is pointing upward in the front and downward in the rear of the rotor. This results in a highly unsteady and complex flow and might be the cause for the local raise in C_T and C_P. As the advance ratio is further increased the velocity component perpendicular to the rotor disk becomes stronger and the entire wake is above the rotor (windmill brake state). This would explain why the increase is limited to $\mu \leq 0.17$. However, the mechanism leading to a raise in C_T and C_P for the recirculating flow state remains unknown.

The results for UPM at $\alpha = 0°$, -10° and -20° are also given in Fig. 16. The comparison with experiment shows that the simulation matches both thrust and power coefficient for -10° and -20° tilt angle. However, the discrepancy from the measurement becomes greater for $\alpha = 0°$, especially for power coefficient. This is because for higher rotor tilt angles the angle of attack at the blade sections are higher and thus the area on the rotor disk where flow separation occurs increases. However, the prediction of flow separation is challenging for UPM.

Finally, the C_{Fy}-μ-diagram is discussed. For $\mu \geq 0.2$ advance ratio is the dominating influencing pa-

rameter on the tangential force coefficient. On the contrary, for $\mu \leq 0.2$ the tilt angle is primarily influencing C_{Fy} and advance ratio has only minor significance. The UPM simulation shows good agreement with the measurement for $\mu \geq 0.2$. For $\mu \leq 0.2$ UPM gives lower tangential force coefficients than the measurement. The linear trend for $\mu \geq 0.2$ is also observable in the UPM calculations for $\mu \leq 0.2$. It is important to note that for low advance ratios the flow around the motor fairing is highly influenced by the rotor wake. Hence, the subtraction of forces obtained with only the aerodynamic fairing from the measurements with fairing and rotor is biased since the assumption of identical flow around the fairing does not hold true. (This error is larger for C_{Fy} than for C_T because the ratio of tangential force acting on the cover compared to the force acting on the rotor is higher than for the thrust direction.) Therefore, the result obtained with UPM for C_{Fy} for $\mu \leq 0.2$ is considered more trustworthy than the measurement.

4.4. Empirical Rotor Model

As described above, the dimensionless coefficients C_T, C_{Fy} and C_P can be used to fully describe lift, drag and power of the rotor as a function of tilt angle and advance ratio. In this section, an empirical model for the CAMcarbon Light rotors is developed based mainly on experimental data. (Only for C_{Fy} and $\mu \leq 0.2$ simulation data are used for the reasons mentioned above.) Since multicopters operate most of the time in hover and steady forward flight the model is developed for $-30° \leq \alpha \leq 0°$. For each dimensionless coefficient an equation is derived (Eq. 9 - Eq. 11, α in degrees). The comparison of the empirical model with the measurement results shows good agreement for all three coefficients (see Fig. 16).

Because the influence of the Reynolds number is not considered in the model, it cannot be applied for all Reynolds numbers. The experiments were performed at Reynolds numbers between 90,000 and 142,000 (calculated at 75% of rotor radius). Studies by Winslow et al.[31] and Mueller et al.[34] showed that for conventional airfoils the lift-to-drag ratio decreases strongly for Reynolds numbers below 100,000 reducing the aerodynamic efficiency of small rotors. Therefore the model is not applicable to rotors with smaller Reynolds numbers. For higher Reynolds numbers, the influence of the Reynolds number on the lift-to-drag ratio is smaller, so that the model is still expected to have good applicability at moderately higher Reynolds numbers than those studied. Furthermore, in all studied cases the flow was incompressible. For this reason, the model

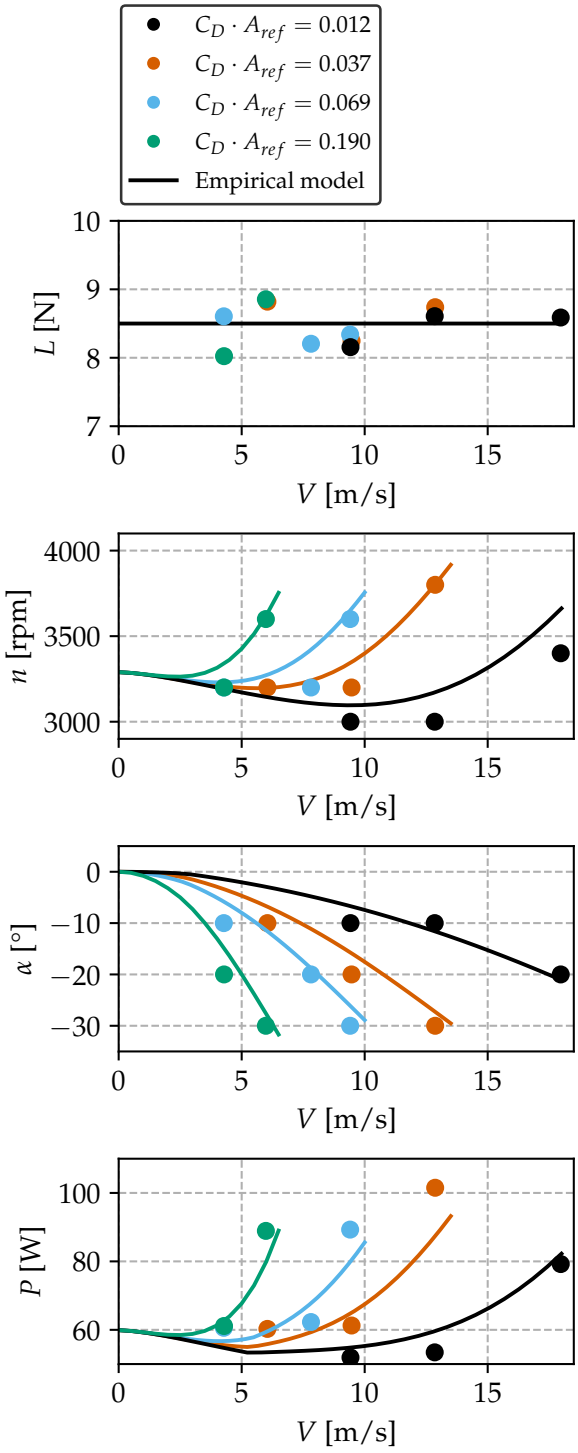

Figure 17: Comparison of the empirical rotor model with the measurement

is also limited to applications with incompressible blade tip flow.

In the following, we will outline how the empirical rotor model can be used in preliminary design of multicopters. Neglecting aerodynamic interactions between the rotors and the fuselage, multicopters can

Empirical rotor model

$$C_T(\mu,\alpha) = 1.14\cdot 10^{-2} + (4.86\cdot 10^{-2} + 3.17\cdot 10^{-3}\alpha)\cdot \mu^{1.5} \tag{9}$$

$$C_{Fy}(\mu,\alpha) = \begin{cases} 0 & \mu \le 0.04 \\ 4.79\cdot 10^{-3}\cdot(\mu - 0.04) & \text{otherwise} \end{cases} \tag{10}$$

$$C_P(\mu,\alpha) = \begin{cases} 1.19\cdot 10^{-3} & \mu \le 0.08 \\ 1.19\cdot 10^{-3} + (2.62\cdot 10^{-3} - 1.26\cdot 10^{-4}\alpha)\cdot(\mu - 0.08) & \text{otherwise} \end{cases} \tag{11}$$

be modeled as a set of i single rotors and a blunt body representing the multicopter's fuselage. The blunt body is characterized by its mass m (payload), the drag coefficient C_D and an aerodynamic reference area A_{ref}. In steady forward flight the weight of the multicopter must be in equilibrium with the sum of lift forces L_i and the drag of the blunt body with the sum of propulsive forces D_i generated by the rotors:

$$\sum_i (\cos(\alpha) C_{T,i} - \sin(\alpha) C_{Fy,i}) \cdot \rho A_i (\Omega_i R_i)^2 = m \cdot g \tag{12}$$

$$\sum_i (\sin(\alpha) C_{T,i} + \cos(\alpha) C_{Fy,i}) \cdot \rho A_i (\Omega_i R_i)^2 = \frac{\rho}{2} V_\infty C_D A_{ref} \tag{13}$$

Moreover, the sum of rotor torques must vanish in stationary flight so that the drone does not rotate:

$$\sum_i C_{P,i} \cdot \rho A_i (\Omega_i R_i)^2 R_i = 0 \tag{14}$$

Besides the mentioned force and torque equilibria there are further ones in the other spatial directions. However, these do not play a role if the multicopters are symmetrically constructed (with exception for pitching moment).

To verify the empirical rotor model, we consider a system consisting of one CAMcarbon Light 16x6 rotor and a blunt body. Since the torque equilibrium cannot be achieved with only one rotor, only Eq. 12 and Eq. 13 are considered. For a constant lift force of 8.5 N provided by the rotor, Fig 17 shows the rotational speed n, rotor tilt angle α and power P as predicted by the empirical rotor model for varying flight velocities and four different blunt bodies ($C_D \cdot A_{ref}$). The prediction of rotor power shows a typical characteristic for helicopters. Starting from hover, the required power initially decreases with increasing airspeed. For higher airspeeds, the required power increases again and exceeds the power in hover. The figure additionally shows results obtained in the measurement presented above that fulfill the trim conditions for lift and propulsive force. The empirical model shows good agreement with the measurement.

Finally, the application of the model is demonstrated on a multicopter configuration. A quadcopter with a mass of 5 kg and four identical rotors with a rotor radius of 0.2 m each is examined. Figure 18 shows the power required by the rotors in forward flight for four different fuselages (the aerodynamic quality is represented by different $C_D \cdot A_{ref}$). The figure illustrates that the aerodynamic quality of the fuselage in this configuration has very little effect on the power consumption for airspeeds below 6 m/s.

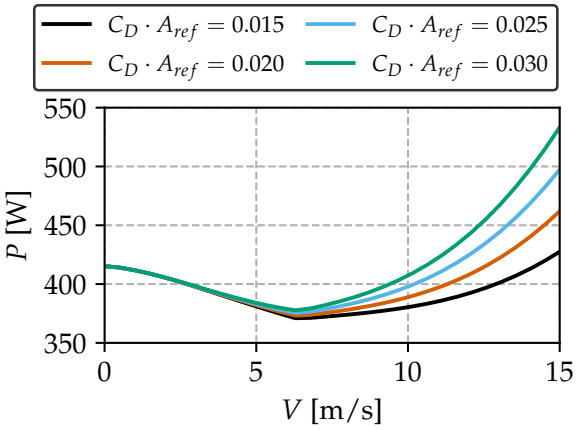

Figure 18: Application of the model to estimate the power consumption of a quadcopter

5. CONCLUSIONS

The major results of this study can be summarized as follows:

- BOS was successfully applied to visualize blade tip vortices of a small-scale rotor (CAMcarbon Light 16x6) for hover and forward flight. Vortex pairing known from helicopter wakes was also found for the small-scale rotor in hover. The empirical wake model of Kocurek and Tangler reproduced the detected vortex trajectories of the studied rotor well.

- In forward flight, the tip vortex trajectories were influenced by rotor tilt angle and advance ratio. The longer the vortices remained in the vicinity of the rotor plane, the more strongly they were affected by the downwash of the following rotor blade. For positive tilt angles the vortices were located above the rotor and were only visible for a vortex age of up to 180° indicating that they were destroyed by the following rotor by BVI.

- The hover performance of eleven rotors was investigated experimentally. Calculations with UPM were carried out for three rotors showing satisfactory agreement with the measurement. In accordance with momentum theory, up to $C_T = 0.012$ the figure of merit for the studied two-bladed rotors increased with increasing thrust coefficient. For higher C_T, the figure of merit decreased since the higher blade pitch led to flow separation and thus to an increase in drag. The comparison of two- and three-bladed rotors revealed that due to the higher rotor solidity, the three-bladed rotors had higher thrust coefficients but also greater parasitic drag and thus smaller figures of merit.

- CAMcarbon Light 16x6 and CAMcarbon Light 12x4.5 rotors were studied in forward flight with varying rotational speed, rotor tilt angle and inflow velocities, covering a wide range of operating conditions. Dimensional analysis states that for forward flight thrust, power and tangential force coefficients depend only on advance ratio and rotor tilt angle. Therefore, both rotors showed the same dependencies.

- Based on the measurements of CAMcarbon Light 16x6 and CAMcarbon Light 12x4.5 in forward flight a simple, empirical model for C_T, C_P and C_{Fy} was developed. It represents the aerodynamic performance of the rotor for $-30° \leq \alpha \leq 0°$ and $\mu < 0.35$ and can be applied in preliminary design of multicopters. The application of the model was demonstrated on a single rotor and a quadrotor configuration.

REFERENCES

[1] Ramasamy, M., Johnson, B., Leishman, J.G., "Understanding the Aerodynamic Efficiency of a Hovering Micro-Rotor", *Journal of the American Helicopter Society*, Vol. **53**, No. 4, 2008, pp. 412-428, DOI: 10.4050/JAHS.53.412.

[2] Ramasamy, M., Lee, T.E., Leishman, J.G., "Flowfield of a Rotating-Wing Micro Air Vehicle", *Journal of Aircraft*, Vol. **44**, No. 4, 2007, pp. 1236-1244, DOI: 10.2514/1.26415.

[3] Hein, B.J., Chopra I., "Hover Performance of a Micro Air Vehicle: Rotors at Low Reynolds Number", *Journal of the American Helicopter Society*, Vol. **52**, No. 3, 2007, pp. 254-262, DOI: 10.4050/JAHS.52.254.

[4] Lakshminarayan, V.K., Baeder, J.D., "Computational Investigation of Micro Hovering Rotor Aerodynamics", *Journal of the American Helicopter Society*, Vol. **55**, No. 2, 2010, p 22001, DOI: 10.4050/JAHS.55.022001.

[5] Ramasamy, M., Gold, N.P., Bhagwat, M.J., "Rotor Hover Performance and Flowfield Measurements with Untwisted and Highly-twisted Blades", *36th European Rotorcraft Forum*, Paris, France, 7-9 Sept. 2010.

[6] Klimczyk, W.A., "Aerodynamic design and optimization of propellers for multirotor", *Aircraft Engineering and Aerospace Technology*, Vol. **94**, No. 1, 2021, pp. 21-30, DOI: 10.1108/AEAT-12-2020-0288.

[7] Bohorquez, F., Pines, D., Samuel, P.D., "Small rotor design optimization using blade element momentum theory and hover tests", *Journal of Aircraft*, Vol. **47**, No. 1, 2010, pp. 268-283, DOI: 10.2514/1.45301.

[8] Milluzzo, J., Leishman, J.G., "Fluid dynamics of the helicoidal wake sheets trailed from a hovering rotor", *Journal of the American Helicopter Society*, Vol. **61**, No. 1, 2016, pp. 1-17, DOI: 10.4050/JAHS.61.012002.

[9] Serrano, D., Ren, M., Qureshi, A.J., Ghaemi, S., "Effect of Disk Angle-of-Attack on Aerodynamic Performance of Small Propellers", *Aerospace Science and Technology*, Vol. **92**, 2019, pp. 901-914, DOI: 10.1016/j.ast.2019.07.022.

[10] Kolaei, A., Barcelos, D., Bramesfeld, G., "Experimental Analysis of a Small-Scale Rotor at Various Inflow Angles", *International Journal of Aerospace Engineering*, 2018, DOI: 10.1155/2018/2560370.

[11] Simmons, B.M., Hatke, D.B., "Investigation of High Incidence Angle Propeller Aerodynamics for Subscale eVTOL Aircraft", NASA/TM-20210014010, 2021.

[12] Krebs, T., Bramesfeld, G., Cole, J., "Transient Thrust Analysis of Rigid Rotors in Forward Flight", *Aerospace*, Vol. **9**, No. 1, 2022, DOI: 10.3390/aerospace9010028.

[13] Theys, B., Dimitriadis, G., Hendrick, P., De Schutter, J., "Experimental and Numerical Study of Micro-Aerial-Vehicle Propeller Performance in Oblique Flow", *Journal of Aircraft*, Vol. **54**, No. 3, 2017, pp. 1076-1084, DOI: 10.2514/1.C033618.

[14] Yang, H., Xia, W., Wang, K., Hu, S., "Aerodynamic performance of a small-scale tilt rotor: Numerical simulation and experiment in steady state", *Proceedings of the Institution of Mechanical Engineers, Part C: Journal of Mechanical Engineering Science*, 2020, DOI: 10.1177/0954406220950352.

[15] Ye, J., Wang, J., He, S., Song, T., "Rotor Performance Analysis and Modeling of Multirotor Using Wind-Tunnel Test", 2020 International Conference on Unmanned Aircraft Systems (ICUAS), Athens, Greece, Sept 1-4, 2020, DOI: 10.1109/ICUAS48674.2020.9214059.

[16] Pollet, F., Delbecq, S., Budinger, M., Moschetta, J.M., "Design optimization of multirotor drones in forward flight", 32nd Congress of the International Council of the Aeronautical Sciences, Shanghai, China, Sept 6-10, 2021.

[17] Ye, J., Wang, J., Song, T., Wu, Z., Tang, P., "Nonlinear Modeling the Quadcopter Considering the Aerodynamic Interaction", *IEEE Access*, Vol. **9**, 2021, pp. 134716-134732, DOI: 10.1109/ACCESS.2021.3116676.

[18] Ghee, T.A., Elliott, J.W., "The Wake of a Small-Scale Rotor in Forward Flight Using Flow Visualization", 48th Annual Forum of the American Helicopter Society, Washington D.C., USA, June 3-5, 1992.

[19] Lößle, F., Kostek, A.A., Schwarz, C., Schmid, R., "Experimental Measurement of a UAV Rotor's Acoustic Emission", *STAB/DGLR Symposium 2020: New Results in Numerical and Experimental Fluid Mechanics XIII*, 2021, pp. 387-396, DOI: 10.1007/978-3-030-79561-0_37.

[20] Schwarz, C., Braukmann, J.N., "Practical aspects of designing background-oriented schieren (BOS) experiments for vortex measurements", Vertical Flight Society's 78th Annual Forum & Technology Display, Fort Worth, TX, USA, May 10-12, 2022.

[21] Russel, C., Conley, S., "The Multirotor Test Bed–A New NASA Test Capability for Advanced VTOL Rotorcraft Configurations", *Vertical Flight Society's 76th Annual Forum & Technology Display*, Virginia Beach, VA, USA, 6-8 Oct. 2020.

[22] Ahmed, S.R., Vidjaja V.T., "Unsteady Panel Method Calculation of Pressure Distribution on BO 105 Model Rotor Blades", *Journal of the American Helicopter Society*, Vol. **43**, No. 1, 1998, pp. 47-56, DOI: 10.4050/JAHS.43.47.

[23] Yin, J., Ahmed S.R., "Helicopter Main-Rotor/Tail-Rotor Interaction", *Journal of the American Helicopter Society*, Vol. **45**, No. 4, 2000, pp. 293-302, DOI: 10.4050/JAHS.45.293.

[24] Yin, J., Ahmed S.R., "Treatment of Unsteady Rotor Aerodynamics", DLR Technical Report, IB 129-94/21, 1994.

[25] Schwarz, C., Bauknecht, A., Wolf, C.C., Coyle, A., Raffel, M., "A Full-Scale Rotor-Wake Investigation of a Free-Flying Helicopter in Ground Effect Using BOS and PIV", *Journal of the American Helicopter Society*, Vol. **65**, No. 3, 2020, pp. 1-2,. DOI: 10.4050/JAHS.65.032007.

[26] Landgrebe, J.L., "The Wake Geometry of a Hovering Helicopter Rotor and Its Influence on Rotor Performance", *Journal of the American Helicopter Society*, Vol. **17**, No. 4, 1972, pp. 2-15.

[27] Kocurek, J.D., Tangler J.L., "A Prescribed Wake Lifting Surface Hover Performance Analysis", *Journal of the American Helicopter Society*, Vol. **22**, No. 1, 1977, pp. 24-35.

[28] Chung, K., Hwang, C., Lee, D., Yim, J., "Numerical Investigation on a Rotor Tip-Vortex Instability in Very Low Advance Ratio Flight", *KSAS International Journal*, Vol. **6**, No. 2, 2005, pp. 84-96, DOI: 10.5139/IJASS.2005.6.2.084.

[29] Leishman, J.G., "Principles of Helicopter Aerodynamics", second edition, Cambridge University Press, New York, NY, 2006.

[30] Drela, M., "XFOIL: An analysis and design system for low Reynolds number airfoils", *Low Reynolds number aerodynamics*, Springer, Berlin, Heidelberg, 1989, pp. 1-12.

[31] Winslow, J., Otsuka, H., Govindarajan, B., Chopra, I., "Basic Understanding of Airfoil Characteristics at Low Reynolds Numbers", *Journal of Aircraft*, Vol. **55**, No. 3, 2018, pp. 1050-1061, DOI: 10.2514/1.C034415.

[32] Kostek, A.A., Lößle, F., Wickersheim, R., Keßler, M., Boisard, R., Reboul, G., Gardner, A.D., "Experimental investigation of UAV rotor aeroacoustics and aerodynamics with computational cross-validation", *48th European Rotorcraft Forum*, Winterthur, Switzerland, 5-9 Sept. 2022.

[33] Anderson, J., "Fundamentals of Aerodynamics", sixth edition, McGraw-Hill, New York, NY, 2017.

[34] Mueller, T.J., "Aerodynamic Measurements at Low Reynolds Numbers for Fixed Wing Micro-Air Vehicles", *RTO AVT/VKI Special Course on Development and Operation of UAVs for Military and Civil Applications*, Brussels, Belgium, 13-17 Sept. 1999.